Journal of
Mechanics of
Materials and Structures

WAVE PROPAGATION IN THREE-DIMENSIONAL GRAPHENE AEROGEL CYLINDRICAL SHELLS RESTING ON WINKLER–PASTERNAK ELASTIC FOUNDATION

Chen Liang and Yan Qing Wang

Volume 15, No. 4 July 2020

msp

JOURNAL OF MECHANICS OF MATERIALS AND STRUCTURES
Vol. 15, No. 4, 2020
https://doi.org/10.2140/jomms.2020.15.435

WAVE PROPAGATION IN THREE-DIMENSIONAL GRAPHENE AEROGEL CYLINDRICAL SHELLS RESTING ON WINKLER–PASTERNAK ELASTIC FOUNDATION

CHEN LIANG AND YAN QING WANG

The objective of this work is to investigate the wave propagation characteristics of circular cylindrical shells made of three-dimensional graphene aerogel (3D-GA). Different distributions of 3D-GA inside the shells are taken into account. The first-order shear deformation (FSD) shell theory is utilized to model the present shells. Hamilton's principle is employed to drive the equations of motion, which governs the wave propagation behavior of 3D-GA cylindrical shells. The analytical wave dispersion relations with longitudinal and circumferential wave numbers are obtained. In addition, detailed parametric studies are conducted to emphasize the influences of the porosity distribution, the porosity coefficient, the radius-to-thickness ratio, the applied forces and the elastic foundation on wave propagation characteristics of 3D-GA cylindrical shells.

1. Introduction

Since the isolation of graphene films was first achieved by Novoselov et al. [2004], this type of carbon materials has been one of the most interesting materials owing to its extraordinary fracture strength, superior Young's modulus, extreme thermal conductivity and so on [Lee et al. 2008; Geim and Novoselov 2009; Chatterjee et al. 2012; Wang et al. 2012; Geim 2009]. Recently, based on several physical and chemical methods, the macroscopic architecture of three-dimensional graphene aerogel (3D-GA) was successfully fabricated by using the controlled micro/nano-scale graphene sheets as building blocks [Vickery et al. 2009; Xu et al. 2010; Chen et al. 2011; Huang et al. 2012; Kuang et al. 2013; Jiang and Fan 2014; Li et al. 2014; Sha et al. 2016; 2017; Strek et al. 2017]. Such creative design make 3D-GA possess many exciting properties, such as high compressibility, super elasticity, extremely low density and electrochemical stability [Chen et al. 2014; Wu et al. 2015; Xu et al. 2016; Qin et al. 2017; Qiu et al. 2017].

As one of the most novel developments in advanced porous structures, 3D-GA structures exhibit tremendous potentials and applications in biological, environmental, electric and chemical engineering. For instance, using 3D-GA structures as the conductive and biocompatible scaffold, it can support neural stem cells (NSCs) growth and keep NSCs at the positive proliferation state [Li et al. 2013]. With the abilities of reversible absorption and discharge of liquids and strong hydrophobicity, 3D-GA structures can be applied for the liquid transfer and environmental cleanup [Wu et al. 2015]. Owing to their high

Wang is the corresponding author.
Keywords: three-dimensional graphene aerogel, cylindrical shell, wave propagation, Winkler–Pasternak elastic foundation, first-order shear deformation theory.

specific surface area, 3D-GA structures were proposed as recyclable and versatile sorbent with the efficient absorption of not only toxic solvents, but also fats and petroleum products [Bi et al. 2012]. It is worth mentioning that the porous structures could be analyzed by using the gradient elasticity [Xu et al. 2008; 2014; Askes and Aifantis 2009; Sun and Aifantis 2014; Aifantis 2016; Lurie et al. 2018].

Investigation of wave propagation characteristics in structures is of significance in practical engineering applications [Wang 2010; Zeighampour et al. 2017; 2018; Zhen 2017]. Zeighampour and Beni [2017] carried out the wave propagation analysis of functionally graded (FG) cylindrical shells reinforced by CNTs. Hu et al. [2008] investigated the transverse and torsional wave propagation in double- and single-walled CNTs. Ma et al. [2018] utilized the classical and FSD shell theories to study wave propagation in magneto-electro-elastic nanoshells. Based on the fast Fourier transform (FFT), Shakeri et al. [2006] investigated wave propagation characteristics in FG thick cylindrical shells subjected to dynamic load. Aminipour et al. [2018] utilized Reddy's higher-order shear deformation theory to study the wave propagation of FG anisotropic doubly-curved shells. Thorp et al. [2005] analyzed the attenuation of wave propagation in fluid-loaded cylindrical shells with periodic shunted piezoelectric rings. Using the three-dimensional theory of anisotropic elasticity, Talebitooti and Choudari Khameneh [2017] analyzed the wave propagation across double-walled laminated composite cylindrical shells along with air-gap. Sorokin and Ershova [2004] studied the plane wave propagation in periodic cylindrical shells with and without fluid loads. The wave propagation analysis in spherically symmetric shells made of laminated piezoelectric materials was carried out in [Dai and Wang 2005]. Here the electric excitation and the thermal shock loads were taken into account. By using the reverberation ray matrix method and the generalized ray method, Liu et al. [2011] investigated the transient elastic wave propagation in laminated composite circular cylindrical shells. The Flügge shell theory was utilized to investigate wave propagation of CNTs in [Wang and Varadan 2007]. Using the Cooper–Naghdi thick shell theory and Love's thin shell theory, Liew and Wang [2007] studied wave propagation in single- and double-walled CNTs.

In this study, wave propagation analysis of circular cylindrical shells made of 3D-GA is carried out for the first time. Different distributions of 3D-GA inside the shells are taken into account. The FSD shell theory and Hamilton's principle are employed to obtain the governing equations. The analytical wave dispersion relations for 3D-GA cylindrical shells are derived. In addition, the influences of several parameters are investigated on the wave propagation in 3D-GA cylindrical shells resting on the Winkler–Pasternak elastic foundation.

2. Material properties of 3D-GA cylindrical shells

A 3D-GA cylindrical shell with the middle-surface radius r and thickness h, subjected to applied axial and circumferential distributed forces N_{px} and $N_{p\theta}$, is shown in Figure 1. Suppose that the shell is resting on the Winkler–Pasternak elastic foundation with spring constant k_w and shear constant k_p. A cylindrical coordinate system (x, θ, z) is set on the middle surface of the shell.

As illustrated in Figure 2, four types of porosity distribution across the shell thickness, namely, porosity-1, porosity-2, porosity-3 and porosity-4, are taken into account.

In the porosity-1 shell, the mass density and elastic moduli have the maxima on the inner and outer surfaces which are equal to corresponding material parameters of solid graphene without internal foams,

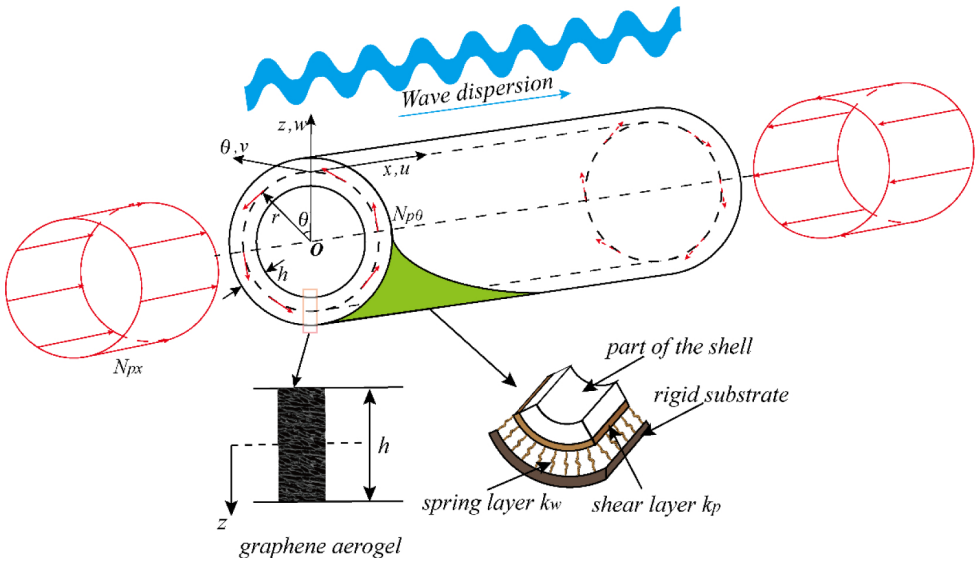

Figure 1. Schematic diagram of 3D-GA cylindrical shell.

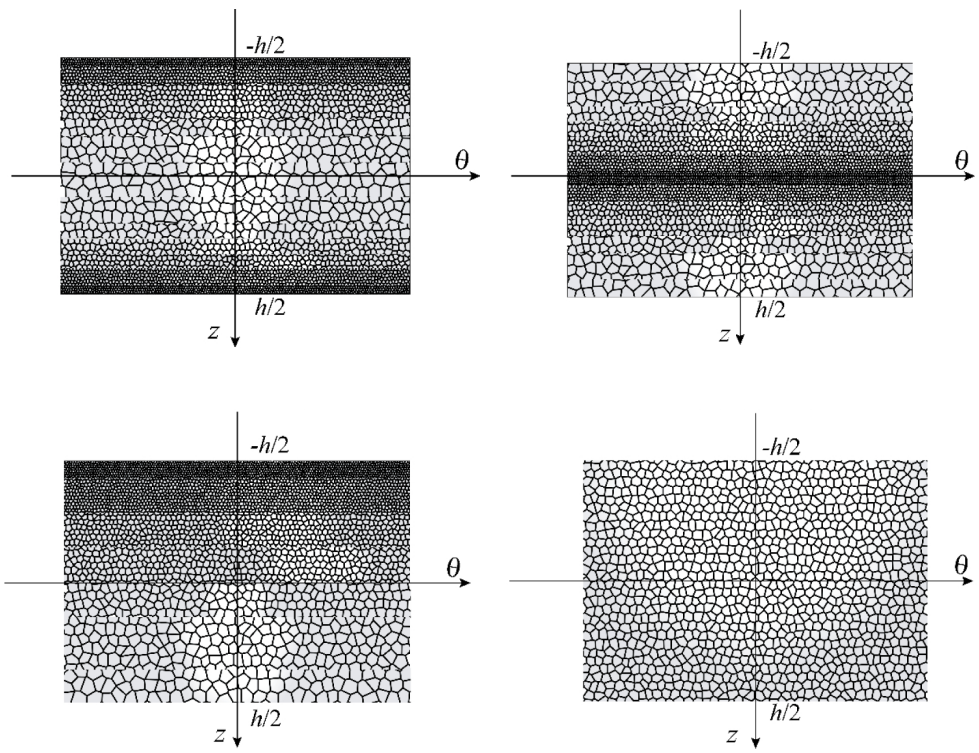

Figure 2. Different types of porosity distribution: porosity-1 (top left), porosity-2 (top right), porosity-3 (bottom left) and porosity-4 (bottom right).

while the mass density and elastic moduli reach the minimum values on the middle-surface owing to the largest size of internal pores. In the porosity-2 shell, the mass density and elastic moduli are the minima on the inner and outer surfaces, while the maxima of mass density and elastic moduli are on the middle-surface. In the porosity-3 shell, mass density and elastic moduli are the minima on the outer surface and increase gradually to the maxima on the inner surface. In the porosity-4 shell, the mass density and elastic moduli remain constant.

Young's modules $E(z)$, shear modules $G(z)$ and mass density $\rho(z)$ for porosity-1, porosity-2, porosity-3 and porosity-4 shells are expressed below [Magnucki and Stasiewicz 2004; Jabbari et al. 2014; Chen et al. 2015; Yang et al. 2018; Wang et al. 2019].

Porosity-1 shell:

$$E(z) = E_g\left[1 - e_1 \cos\frac{\pi z}{h}\right], \tag{1a}$$

$$G(z) = G_g\left[1 - e_1 \cos\frac{\pi z}{h}\right], \tag{1b}$$

$$\rho(z) = \rho_g\left[1 - e_1^* \cos\frac{\pi z}{h}\right]. \tag{1c}$$

Porosity-2 shell:

$$E(z) = E_g\left\{1 - e_2\left[1 - \cos\frac{\pi z}{h}\right]\right\}, \tag{2a}$$

$$G(z) = G_g\left\{1 - e_2\left[1 - \cos\frac{\pi z}{h}\right]\right\}, \tag{2b}$$

$$\rho(z) = \rho_g\left\{1 - e_2^*\left[1 - \cos\frac{\pi z}{h}\right]\right\}. \tag{2c}$$

Porosity-3 shell:

$$E(z) = E_g\left[1 - e_3 \cos\left(\frac{\pi z}{2h} + \frac{\pi}{4}\right)\right], \tag{3a}$$

$$G(z) = G_g\left[1 - e_3 \cos\left(\frac{\pi z}{2h} + \frac{\pi}{4}\right)\right], \tag{3b}$$

$$\rho(z) = \rho_g\left[1 - e_3^* \cos\left(\frac{\pi z}{2h} + \frac{\pi}{4}\right)\right]. \tag{3c}$$

Porosity-4 shell:

$$E(z) = E_g\,\zeta, \tag{4a}$$

$$G(z) = G_g\,\zeta, \tag{4b}$$

$$\rho(z) = \rho_g\,\zeta^*, \tag{4c}$$

where the maximum value of Young's modules, shear modules and mass density are E_g, G_g and ρ_g, respectively; e_1, e_2 and e_3 $(0 \le e_1,\ e_2,\ e_3 < 1)$ are porosity coefficients for the porosity-1, porosity-2 and porosity-3 shells, respectively; and the corresponding coefficients of mass density are e_1^*, e_2^* and e_3^*; ζ and ζ^* are corresponding coefficients for the porosity-4 shell. The shear modulus is given by

$$G(z) = \frac{E(z)}{2(1+\mu)}, \tag{5}$$

where Poisson's ratio μ is a constant.

For the graphene aerogel with open-cell foams, the relationship of the material properties is provided as [Qin et al. 2017]

$$\frac{E(z)}{E_g} = \left[\frac{\rho(z)}{\rho_g}\right]^{2.73}. \tag{6}$$

Therefore, the relationships between porosity coefficients and mass density coefficients can be expressed as

$$1 - e_1^* \cos\frac{\pi z}{h} = \sqrt[2.73]{1 - e_1 \cos\frac{\pi z}{h}}, \tag{7}$$

$$1 - e_2^*\left[1 - \cos\frac{\pi z}{h}\right] = \sqrt[2.73]{1 - e_2\left[1 - \cos\frac{\pi z}{h}\right]}, \tag{8}$$

$$1 - e_3^* \cos\left(\frac{\pi z}{2h} + \frac{\pi}{4}\right) = \sqrt[2.73]{1 - e_3 \cos\left(\frac{\pi z}{2h} + \frac{\pi}{4}\right)}, \tag{9}$$

$$\zeta^* = \sqrt[2.73]{\zeta}. \tag{10}$$

Without the loss of generality, let the masses of 3D-GA cylindrical shells with different porosity distributions keep equal to each other. Hence, we obtain [Yang et al. 2018]

$$\int_{-h/2}^{h/2} \sqrt[2.73]{1 - e_1 \cos\frac{\pi z}{h}}\, \mathrm{d}z = \int_{-h/2}^{h/2} \sqrt[2.73]{1 - e_2\left[1 - \cos\frac{\pi z}{h}\right]}\, \mathrm{d}z, \tag{11}$$

$$\int_{-h/2}^{h/2} \sqrt[2.73]{1 - e_1 \cos\frac{\pi z}{h}}\, \mathrm{d}z = \int_{-h/2}^{h/2} \sqrt[2.73]{1 - e_3 \cos\left(\frac{\pi z}{2h} + \frac{\pi}{4}\right)}\, \mathrm{d}z, \tag{12}$$

$$\int_{-h/2}^{h/2} \sqrt[2.73]{1 - e_1 \cos\frac{\pi z}{h}}\, \mathrm{d}z = \int_{-h/2}^{h/2} \sqrt[2.73]{\zeta}\, \mathrm{d}z, \tag{13}$$

which means that the values of e_2, e_3 and ζ can be calculated by a given e_1. As observed in Figure 3, the increase of e_1 leads to the increase of e_2 and e_3 and the decrease of ζ. When $e_1 = 0.6$, e_2 approaches the upper limit. Therefore, the range of e_1 $(0 \le e_1 \le 0.6)$ is selected in the following calculations.

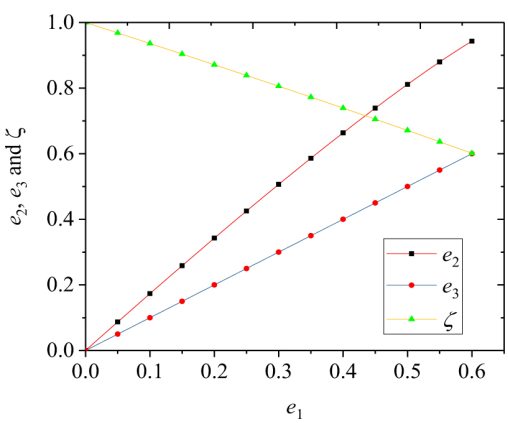

Figure 3. Variations of porosity coefficients for different porosity distributions.

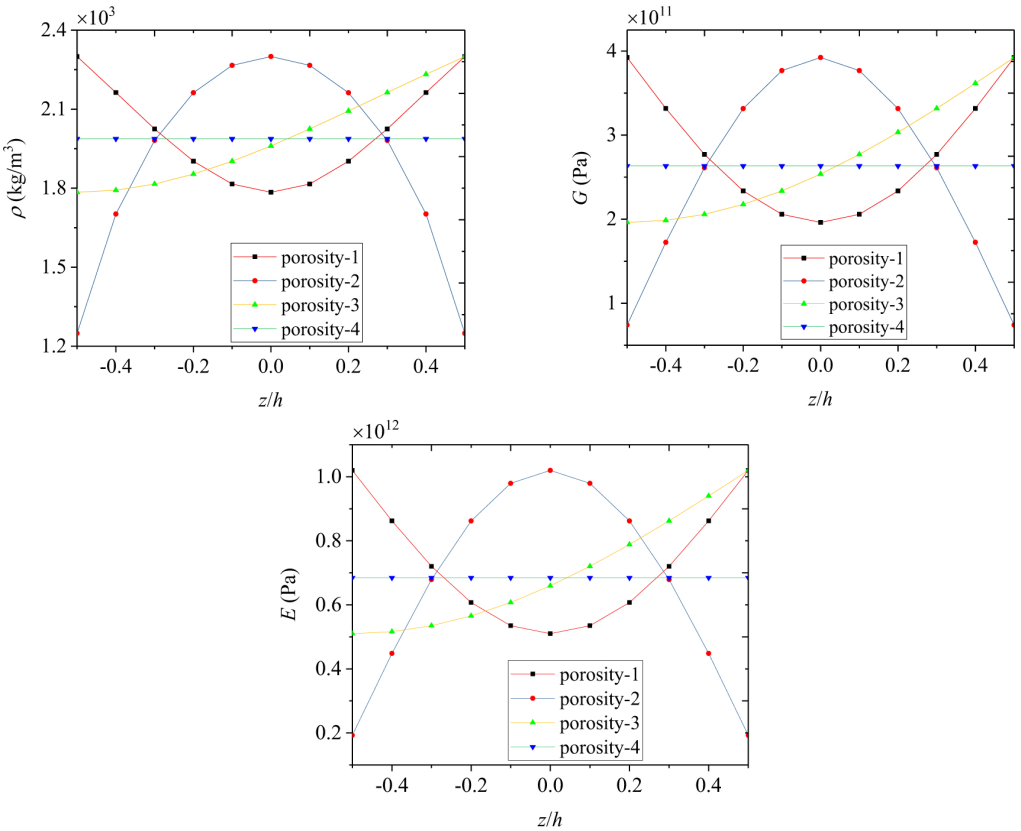

Figure 4. Variations of material properties along the radial direction: mass density (top left), shear modulus (top right) and Young's modulus (bottom).

In Figure 4, the changing curves of mass density, shear modulus and Young's modulus along the radial direction are depicted for porosity-1, porosity-2, porosity-3 and porosity-4 shells, respectively. Herein the following parameters are utilized: $E_g = 1.02\,\text{TPa},\ \mu = 0.3,\ \rho_g = 2300\,\text{kg/m}^3,\ e_0 = 0.5,\ h = 0.1\,\text{m},\ r = 0.3\,\text{m}$.

3. Wave propagation via FSD shell theory

On the basis of the FSD shell theory [Reddy 2004], the displacement field of an arbitrary point in the shell along the x-, θ- and z-axes, denoted by $u_x(x,\theta,z,t),\ v_\theta(x,\theta,z,t)$ and $w_z(x,\theta,z,t)$ are

$$u_x(x,\theta,z,t) = u(x,\theta,t) + z\phi_x(x,\theta,t), \tag{14}$$

$$v_\theta(x,\theta,z,t) = v(x,\theta,t) + z\phi_\theta(x,\theta,t), \tag{15}$$

$$w_z(x,\theta,z,t) = w(x,\theta,t), \tag{16}$$

where $u(x,\theta,t),\ v(x,\theta,t)$ and $w(x,\theta,t)$ are the displacements of a point at the midplane; t is time; $\phi_x(x,\theta,t)$ and $\phi_\theta(x,\theta,t)$ denote the rotations of a transverse normal about the θ- and x-axes, respectively.

The relations between strains and displacements can be written as

$$\varepsilon_x = \frac{\partial u}{\partial x} + z\frac{\partial \phi_x}{\partial x}, \tag{17}$$

$$\varepsilon_\theta = \frac{1}{r}\left(\frac{\partial v}{\partial \theta} + w\right) + \frac{z}{r}\frac{\partial \phi_\theta}{\partial \theta}, \tag{18}$$

$$\gamma_{x\theta} = \frac{\partial v}{\partial x} + \frac{1}{r}\frac{\partial u}{\partial \theta} + z\left(\frac{\partial \phi_\theta}{\partial x} + \frac{1}{r}\frac{\partial \phi_x}{\partial \theta}\right), \tag{19}$$

$$\gamma_{xz} = \phi_x + \frac{\partial w}{\partial x}, \tag{20}$$

$$\gamma_{\theta z} = \phi_\theta + \frac{1}{r}\frac{\partial w}{\partial \theta} - \frac{v}{r}. \tag{21}$$

The relations between stresses and strains can be given by [Reddy 2004]

$$\sigma_x = \frac{E(z)}{1-\mu^2}(\varepsilon_x + \mu\varepsilon_\theta), \tag{22}$$

$$\sigma_\theta = \frac{E(z)}{1-\mu^2}(\varepsilon_\theta + \mu\varepsilon_x), \tag{23}$$

$$\tau_{x\theta} = G(z)\,\gamma_{x\theta}, \tag{24}$$

$$\tau_{xz} = G(z)\,\gamma_{xz}, \tag{25}$$

$$\tau_{\theta z} = G(z)\,\gamma_{\theta z}. \tag{26}$$

The resultant moments and forces are expressed as

$$\begin{Bmatrix} N_x \\ N_\theta \\ N_{x\theta} \end{Bmatrix} = \int_{-h/2}^{h/2} \begin{Bmatrix} \sigma_x \\ \sigma_\theta \\ \tau_{x\theta} \end{Bmatrix} \mathrm{d}z, \tag{27}$$

$$\begin{Bmatrix} M_x \\ M_\theta \\ M_{x\theta} \end{Bmatrix} = \int_{-h/2}^{h/2} \begin{Bmatrix} \sigma_x \\ \sigma_\theta \\ \tau_{x\theta} \end{Bmatrix} z\,\mathrm{d}z, \tag{28}$$

$$\begin{Bmatrix} Q_{\theta z} \\ Q_{xz} \end{Bmatrix} = \kappa_s \int_{-h/2}^{h/2} \begin{Bmatrix} \tau_{\theta z} \\ \tau_{xz} \end{Bmatrix} \mathrm{d}z, \tag{29}$$

where the shear correction coefficient is $\kappa_s = 5/6$ [Reddy 2004].

From (17)–(29), we obtain

$$N_x = A_{11}\frac{\partial u}{\partial x} + A_{12}\frac{\partial \phi_x}{\partial x} + A_{13}\frac{1}{r}\left(\frac{\partial v}{\partial \theta} + w\right) + A_{14}\frac{1}{r}\frac{\partial \phi_\theta}{\partial \theta}, \tag{30}$$

$$N_\theta = A_{11}\frac{1}{r}\left(\frac{\partial v}{\partial \theta} + w\right) + A_{12}\frac{1}{r}\frac{\partial \phi_\theta}{\partial \theta} + A_{13}\frac{\partial u}{\partial x} + A_{14}\frac{\partial \phi_x}{\partial x}, \tag{31}$$

$$N_{x\theta} = B_{11}\left(\frac{\partial v}{\partial x} + \frac{1}{r}\frac{\partial u}{\partial \theta}\right) + B_{12}\left(\frac{\partial \phi_\theta}{\partial x} + \frac{1}{r}\frac{\partial \phi_x}{\partial \theta}\right), \tag{32}$$

$$M_x = C_{11}\frac{\partial u}{\partial x} + C_{12}\frac{\partial \phi_x}{\partial x} + C_{13}\frac{1}{r}\left(\frac{\partial v}{\partial \theta} + w\right) + C_{14}\frac{1}{r}\frac{\partial \phi_\theta}{\partial \theta}, \tag{33}$$

$$M_\theta = C_{11}\frac{1}{r}\left(\frac{\partial v}{\partial \theta} + w\right) + C_{12}\frac{1}{r}\frac{\partial \phi_\theta}{\partial \theta} + C_{13}\frac{\partial u}{\partial x} + C_{14}\frac{\partial \phi_x}{\partial x}, \tag{34}$$

$$M_{x\theta} = D_{11}\left(\frac{\partial v}{\partial x} + \frac{1}{r}\frac{\partial u}{\partial \theta}\right) + D_{12}\left(\frac{\partial \phi_\theta}{\partial x} + \frac{1}{r}\frac{\partial \phi_x}{\partial \theta}\right), \tag{35}$$

$$Q_{xz} = \kappa_s B_{11}\left(\phi_x + \frac{\partial w}{\partial x}\right), \tag{36}$$

$$Q_{\theta z} = \kappa_s B_{11}\left(\phi_\theta + \frac{1}{r}\frac{\partial w}{\partial \theta} - \frac{v}{r}\right), \tag{37}$$

where the parameters A_{ij}, B_{ij}, C_{ij} and D_{ij} $(i, j = 1, 2, 3, 4)$ are given in Appendix A.

The strain energy of the 3D-GA shell is written as

$$S = \frac{1}{2}\int_0^L\int_0^{2\pi}\int_{-h/2}^{h/2}(\sigma_x\,\varepsilon_x + \sigma_\theta\,\varepsilon_\theta + \tau_{x\theta}\,\gamma_{x\theta} + \tau_{xz}\,\gamma_{xz} + \tau_{\theta z}\,\gamma_{\theta z})\,r\,\mathrm{d}z\,\mathrm{d}\theta\,\mathrm{d}x. \tag{38}$$

The kinetic energy is represented as

$$K = \frac{1}{2}\int_0^L\int_0^{2\pi}\int_{-h/2}^{h/2}\rho(z)\left[\left(\frac{\partial u}{\partial t} + z\frac{\partial \phi_x}{\partial t}\right)^2 + \left(\frac{\partial v}{\partial t} + z\frac{\partial \phi_\theta}{\partial t}\right)^2 + \left(\frac{\partial w}{\partial t}\right)^2\right] r\,\mathrm{d}z\,\mathrm{d}\theta\,\mathrm{d}x. \tag{39}$$

The work done by the applied forces can be expressed as

$$W_F = \frac{1}{2}\int_0^L\int_0^{2\pi}\left[N_{px}\left(\frac{\partial w}{\partial x}\right)^2 + N_{p\theta}\left(\frac{1}{r}\frac{\partial w}{\partial \theta}\right)^2\right] r\,\mathrm{d}\theta\,\mathrm{d}x, \tag{40}$$

where the applied axial and circumferential distributed forces are given by

$$N_{px} = N_{p\theta} = N_p. \tag{41}$$

The additional strain energy results from the Winkler–Pasternak elastic foundation is written as [Winkler 1867; Pasternak 1954]

$$W_G = \frac{1}{2}\int_0^L\int_0^{2\pi}\left\{k_w\,w^2 + k_p\left[\left(\frac{\partial w}{\partial x}\right)^2 + \left(\frac{1}{r}\frac{\partial w}{\partial \theta}\right)^2\right]\right\} r\,\mathrm{d}\theta\,\mathrm{d}x. \tag{42}$$

By employing Hamilton's principle

$$\int_0^t [\delta K - (\delta S + \delta W_F + \delta W_G)]\,\mathrm{d}t = 0, \tag{43}$$

the governing equations of the 3D-GA shell can be obtained as

$$\frac{\partial N_x}{\partial x}+\frac{1}{r}\frac{\partial N_{x\theta}}{\partial \theta}=I_1\frac{\partial^2 u}{\partial t^2}+I_2\frac{\partial^2 \phi_x}{\partial t^2}, \tag{44}$$

$$\frac{\partial N_{x\theta}}{\partial x}+\frac{1}{r}\frac{\partial N_{\theta}}{\partial \theta}+\frac{Q_{\theta z}}{r}=I_1\frac{\partial^2 v}{\partial t^2}+I_2\frac{\partial^2 \phi_\theta}{\partial t^2}, \tag{45}$$

$$\frac{\partial Q_{xz}}{\partial x}+\frac{1}{r}\frac{\partial Q_{\theta z}}{\partial \theta}-\frac{N_\theta}{r}+N_{px}\frac{\partial^2 w}{\partial x^2}+N_{p\theta}\frac{1}{r^2}\frac{\partial^2 w}{\partial \theta^2}-k_w w+k_p\left(\frac{\partial^2 w}{\partial x^2}+\frac{1}{r^2}\frac{\partial^2 w}{\partial \theta^2}\right)=I_1\frac{\partial^2 w}{\partial t^2}, \tag{46}$$

$$\frac{\partial M_x}{\partial x}+\frac{1}{r}\frac{\partial M_{x\theta}}{\partial \theta}-Q_{xz}=I_2\frac{\partial^2 u}{\partial t^2}+I_3\frac{\partial^2 \phi_x}{\partial t^2}, \tag{47}$$

$$\frac{\partial M_{x\theta}}{\partial x}+\frac{1}{r}\frac{\partial M_{\theta}}{\partial \theta}-Q_{\theta z}=I_2\frac{\partial^2 v}{\partial t^2}+I_3\frac{\partial^2 \phi_\theta}{\partial t^2}, \tag{48}$$

where the coefficients I_1, I_2 and I_3 take the form of

$$I_1=\int_{-h/2}^{h/2}\rho(z)\,\mathrm{d}z, \tag{49}$$

$$I_2=\int_{-h/2}^{h/2}\rho(z)\,z\,\mathrm{d}z, \tag{50}$$

$$I_3=\int_{-h/2}^{h/2}\rho(z)\,z^2\,\mathrm{d}z. \tag{51}$$

By substituting (30)–(37) into (44)–(48), it yields

$$A_{11}\frac{\partial^2 u}{\partial x^2}+A_{12}\frac{\partial^2 \phi_x}{\partial x^2}+\frac{A_{13}}{r}\left(\frac{\partial w}{\partial x}+\frac{\partial^2 v}{\partial x\,\partial \theta}\right)+\frac{A_{14}}{r}\frac{\partial^2 \phi_\theta}{\partial x\,\partial \theta}+B_{11}\left(\frac{1}{r^2}\frac{\partial^2 u}{\partial \theta^2}+\frac{1}{r}\frac{\partial^2 v}{\partial x\,\partial \theta}\right)$$
$$+B_{12}\left(\frac{1}{r^2}\frac{\partial^2 \phi_x}{\partial \theta^2}+\frac{1}{r}\frac{\partial^2 \phi_\theta}{\partial x\,\partial \theta}\right)=I_1\frac{\partial^2 u}{\partial t^2}+I_2\frac{\partial^2 \phi_x}{\partial t^2}, \tag{52}$$

$$\frac{A_{11}}{r^2}\left(\frac{\partial^2 v}{\partial \theta^2}+\frac{\partial w}{\partial \theta}\right)+\frac{A_{12}}{r^2}\frac{\partial^2 \phi_\theta}{\partial \theta^2}+\frac{A_{13}}{r}\frac{\partial^2 u}{\partial x\,\partial \theta}+\frac{A_{14}}{r}\frac{\partial^2 \phi_x}{\partial x\,\partial \theta}+B_{12}\left(\frac{1}{r}\frac{\partial^2 \phi_x}{\partial x\,\partial \theta}+\frac{\partial^2 \phi_\theta}{\partial x^2}\right)$$
$$+B_{11}\left(\frac{1}{r}\frac{\partial^2 u}{\partial x\,\partial \theta}+\frac{\partial^2 v}{\partial x^2}+\frac{\kappa_s}{r^2}\frac{\partial w}{\partial \theta}+\frac{\kappa_s}{r}\phi_\theta-\frac{\kappa_s}{r^2}v\right)=I_1\frac{\partial^2 v}{\partial t^2}+I_2\frac{\partial^2 \phi_\theta}{\partial t^2}, \tag{53}$$

$$A_{11}\frac{1}{r^2}\left(w+\frac{\partial v}{\partial \theta}\right)+A_{12}\frac{1}{r^2}\frac{\partial \phi_\theta}{\partial \theta}+A_{13}\frac{1}{r}\frac{\partial u}{\partial x}+A_{14}\frac{1}{r}\frac{\partial \phi_x}{\partial x}$$
$$+\kappa_s B_{11}\left(\frac{\partial \phi_x}{\partial x}+\frac{\partial^2 w}{\partial x^2}+\frac{1}{r^2}\frac{\partial^2 w}{\partial \theta^2}+\frac{1}{r}\frac{\partial \phi_\theta}{\partial \theta}-\frac{1}{r^2}\frac{\partial v}{\partial \theta}\right)+N_{px}\frac{\partial^2 w}{\partial x^2}+\frac{N_{p\theta}}{r^2}\frac{\partial^2 w}{\partial \theta^2}$$
$$-k_w w+k_p\left(\frac{\partial^2 w}{\partial x^2}+\frac{1}{r^2}\frac{\partial^2 w}{\partial \theta^2}\right)=I_1\frac{\partial^2 w}{\partial t^2} \tag{54}$$

$$-B_{11}\kappa_s\left(\phi_x+\frac{\partial w}{\partial x}\right)+C_{11}\frac{\partial^2 u}{\partial x^2}+C_{12}\frac{\partial^2\phi_x}{\partial x^2}+C_{13}\frac{1}{r}\left(\frac{\partial w}{\partial x}+\frac{\partial^2 v}{\partial x\,\partial\theta}\right)+C_{14}\frac{1}{r}\frac{\partial^2\phi_\theta}{\partial x\,\partial\theta}$$
$$+D_{11}\left(\frac{1}{r^2}\frac{\partial^2 u}{\partial\theta^2}+\frac{1}{r}\frac{\partial^2 v}{\partial x\,\partial\theta}\right)+D_{12}\left(\frac{1}{r^2}\frac{\partial^2\phi_x}{\partial\theta^2}+\frac{1}{r}\frac{\partial^2\phi_\theta}{\partial x\,\partial\theta}\right)=I_2\frac{\partial^2 u}{\partial t^2}+I_3\frac{\partial^2\phi_x}{\partial t^2}, \quad (55)$$

$$\kappa_s B_{11}\left(\frac{v}{r}-\frac{1}{r}\frac{\partial w}{\partial\theta}-\phi_\theta\right)+\frac{C_{11}}{r^2}\left(\frac{\partial w}{\partial\theta}+\frac{\partial^2 v}{\partial\theta^2}\right)+\frac{C_{12}}{r^2}\frac{\partial^2\phi_\theta}{\partial\theta^2}+\frac{C_{13}}{r}\frac{\partial^2 u}{\partial x\,\partial\theta}+\frac{C_{14}}{r}\frac{\partial^2\phi_x}{\partial x\,\partial\theta}$$
$$+D_{11}\left(\frac{1}{r}\frac{\partial^2 u}{\partial x\,\partial\theta}+\frac{\partial^2 v}{\partial x^2}\right)+D_{12}\left(\frac{1}{r}\frac{\partial^2\phi_x}{\partial x\,\partial\theta}+\frac{\partial^2\phi_\theta}{\partial x^2}\right)=I_2\frac{\partial^2 v}{\partial t^2}+I_3\frac{\partial^2\phi_\theta}{\partial t^2}. \quad (56)$$

The wave propagation solutions of (52)–(56) are expressed as

$$u(x,\theta,t)=Ue^{\mathrm{i}(kx+n\theta-\omega t)}, \quad (57)$$
$$v(x,\theta,t)=Ve^{\mathrm{i}(kx+n\theta-\omega t)}, \quad (58)$$
$$w(x,\theta,t)=We^{\mathrm{i}(kx+n\theta-\omega t)}, \quad (59)$$
$$\phi_x(x,\theta,t)=\Phi_x\,e^{\mathrm{i}(kx+n\theta-\omega t)}, \quad (60)$$
$$\phi_\theta(x,\theta,t)=\Phi_\theta\,e^{\mathrm{i}(kx+n\theta-\omega t)}, \quad (61)$$

where $\mathrm{i}=\sqrt{-1}$; k and n are the wave numbers in the longitudinal and circumferential directions, respectively; ω is the frequency of wave motion; U, V, W, Φ_x and Φ_θ are the amplitudes of wave motion.

Substituting (57)–(61) into (52)–(56) yields a generalized eigenvalue problem:

$$(L_{5\times5}-\omega^2 H_{5\times5})\begin{Bmatrix}U\\V\\W\\\Phi_x\\\Phi_\theta\end{Bmatrix}=\{0\}, \quad (62)$$

where the elements L_{ij} and H_{ij} $(i,j=1,2,\ldots,5)$ in the matrix $L_{5\times5}$ and $H_{5\times5}$ can be found in Appendix B.

The dispersion relation derived from (62) takes the form of

$$\mathrm{Det}[L_{5\times5}-\omega^2 H_{5\times5}]=0. \quad (63)$$

The relation between the wave frequency ω and phase velocity v is [Wang and Varadan 2007]

$$v=\omega/k. \quad (64)$$

According to (63) and (64), five positive analytical solutions of wave phase velocity can be obtained. The first three low-value solutions which correspond to the coupled longitudinal, radial and circumferential (L-R-C) modes are discussed hereinbelow.

4. Results and discussion

For the purpose of demonstrating the effectiveness of the present analysis, Figure 5 presents a comparative study of the dispersion relation between phase velocity and circumferential wave number for a homogeneous cylindrical shell. The present 3D-GA cylindrical shell model can be simplified to a homogeneous cylindrical shell by setting $N_p = 0\,\mathrm{N}$, $k_w = 0\,\mathrm{N/m^3}$, $k_p = 0\,\mathrm{N/m}$ and $e_1 = 0$. The thickness, the middle-surface radius, Poisson's ratio and the mass density of the cylindrical shell are $h = 0.34\,\mathrm{nm}$, $r = 5\,\mathrm{nm}$, $\mu = 0.2$ and $\rho = 2.27\,\mathrm{g/cm^3}$, respectively. The bending rigidity is $D = 2\,\mathrm{eV}$ and the in-plane stiffness is $Eh = 360\,\mathrm{J/m^2}$. The results from the classical shell theory were given in [Wang and Varadan 2007]. The present results have good consistency with those in the literature, manifesting the effectiveness of the present analysis.

Hereinafter, the wave propagation analysis in 3D-GA cylindrical shells is conducted. If not specified, the following geometric and material parameters are utilized: $h = 0.1\,\mathrm{m}$, $r = 0.3\,\mathrm{m}$, $E_g = 1.02\,\mathrm{TPa}$, $\rho_g = 2300\,\mathrm{kg/m^3}$ and $\mu = 0.3$.

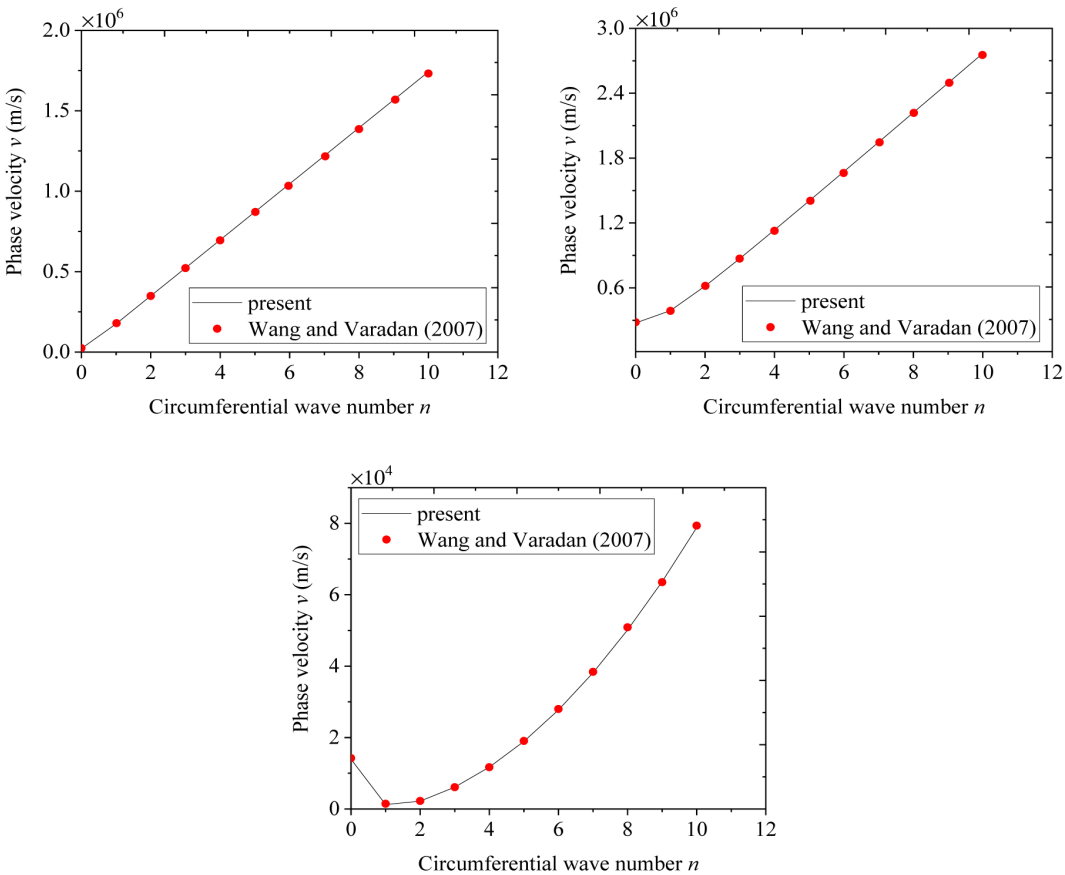

Figure 5. Comparisons of wave characteristics in a homogenous cylindrical shell ($k = 8 \times 10^6\,\mathrm{m^{-1}}$, $e_0 a = 0$): the first mode (top left), the second mode (top right) and the third mode (bottom).

Figure 6 demonstrates the curves of phase velocity versus longitudinal wave number k of 3D-GA shells for the L-R-C modes. Dispersion relations are investigated for porosity-1, porosity-2, porosity-3 and porosity-4 shells. For clearer discussion, we define the mode number by the numerical order of phase velocity in the following results, which is different from Figure 5. As can be observed, for all porosity distributions, the phase velocity for the first L-R-C mode fluctuates initially and then tends to be constant. As for the second and third L-R-C modes, the phase velocities initially exhibit a decreasing trend and then tend to be constant. The nonlinear variation of phase velocities is because the coupling exists among the longitudinal, radial and circumferential wave modes, which arises from the coupled displacement fields. It is worth mentioning that at the larger longitudinal wave number $k > 10^2\,\mathrm{m}^{-1}$, or at corresponding smaller longitudinal wavelength $\lambda = 1/k < 0.01\,\mathrm{m}$, all the phase velocities for the L-R-C modes are close to each other.

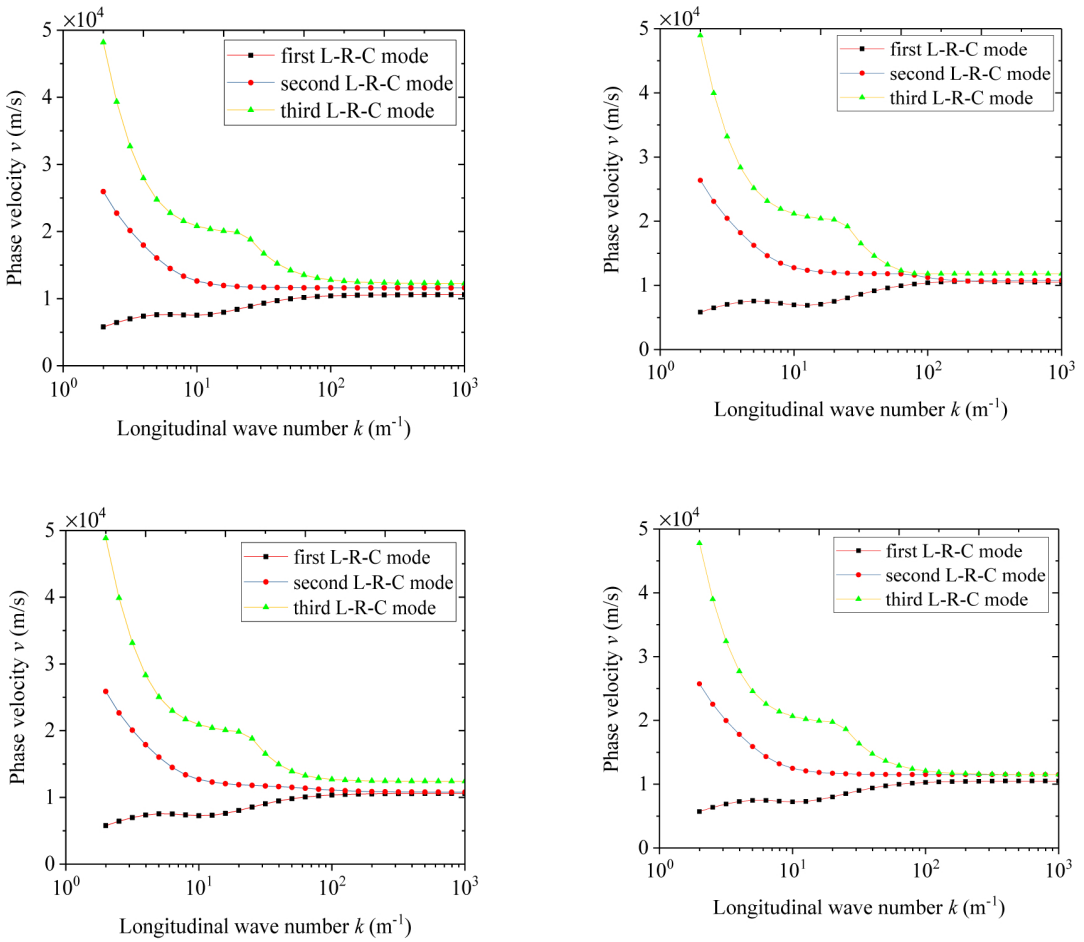

Figure 6. Phase velocity versus longitudinal wave number k of 3D-GA shell ($e_1 = 0.5$, $n = 1$, $N_p = 0\,\mathrm{N}$, $k_w = 0\,\mathrm{N/m^3}$, $k_p = 0\,\mathrm{N/m}$): porosity-1 (top left), porosity-2 (top right), porosity-3 (bottom left) and porosity-4 (bottom right).

In Figure 7, the dispersion relations between the phase velocity and circumferential wave number n for different porosity distributions are shown. It is found that for the first L-R-C mode, the phase velocity decreases initially and then increases with the circumferential wave number. Moreover, the lowest phase velocity occurs at $n = 2$. As for the second and third L-R-C modes, the phase velocities exhibit an increasing-trend variation with increasing circumferential wave number.

Figure 8 depicts the effect of porosity coefficient e_1 on the dispersion relations for different porosity distributions. One can find that the phase velocities in the 3D-GA shell decrease with the increasing porosity coefficient. Among all types of porosity distribution, the porosity-1 shell has the largest phase velocity and the porosity-2 shell has the smallest phase velocity. Moreover, the phase velocity in the porosity-4 shell is smaller than that in the porosity-3 shell.

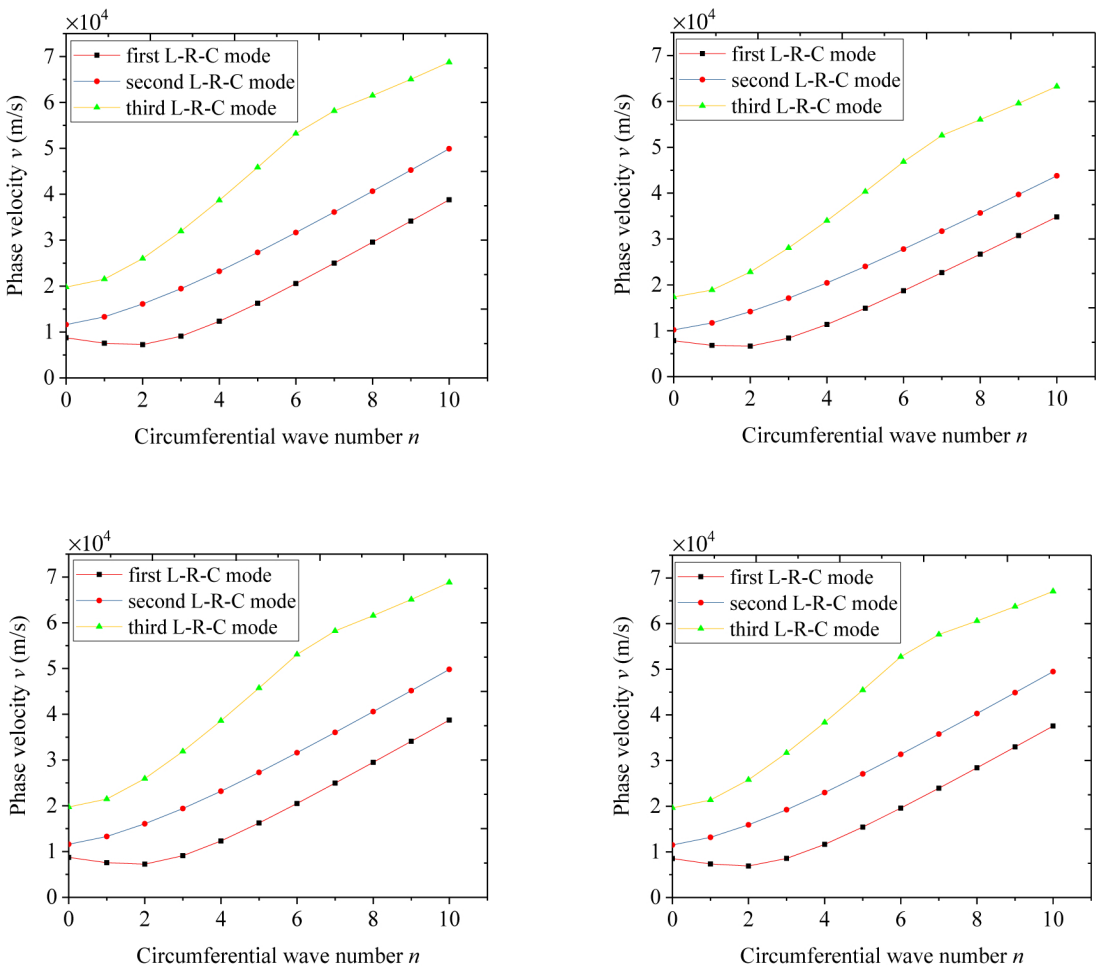

Figure 7. Phase velocity versus circumferential wave number n of 3D-GA shell ($e_1 = 0.5$, $k = 8\,\mathrm{m}^{-1}$, $N_p = 0\,\mathrm{N}$, $k_w = 0\,\mathrm{N/m^3}$, $k_p = 0\,\mathrm{N/m}$): porosity-1 (top left), porosity-2 (top right), porosity-3 (bottom left) and porosity-4 (bottom right).

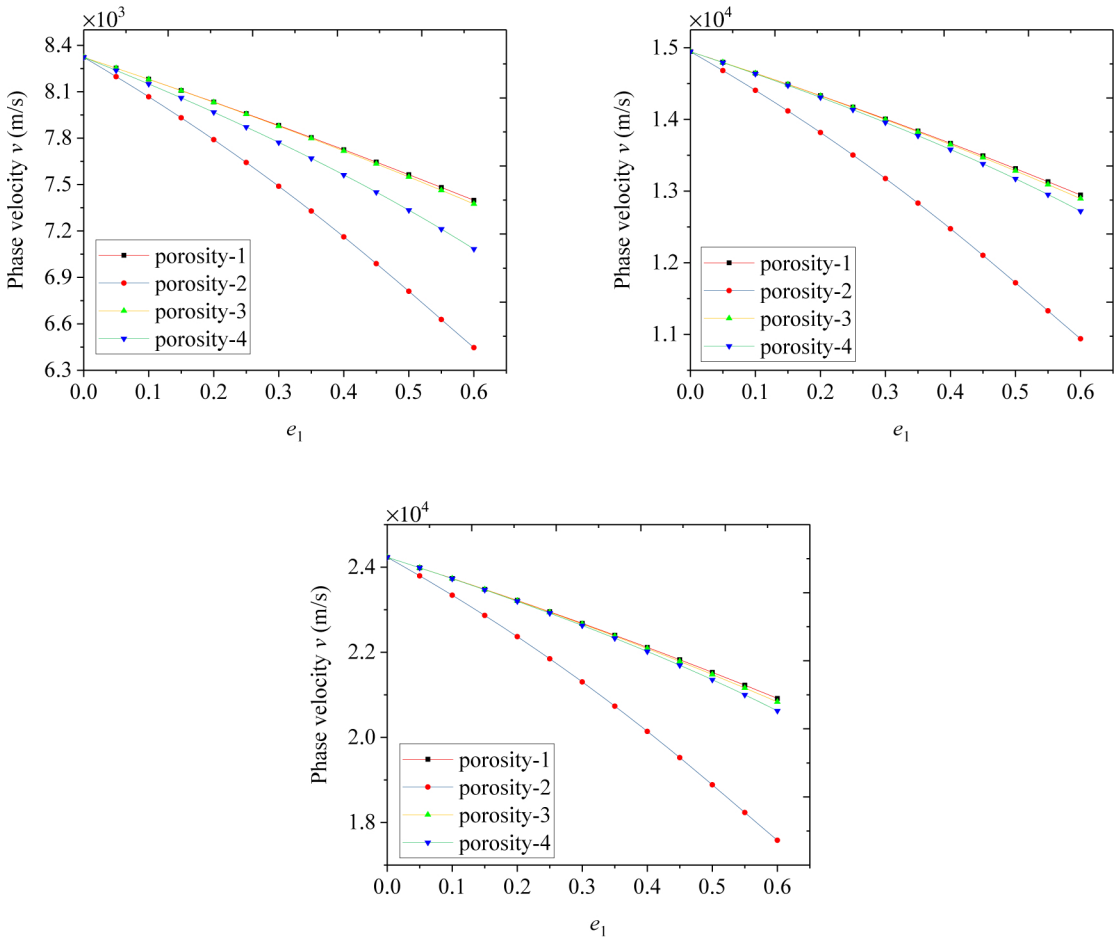

Figure 8. Phase velocity versus porosity coefficient e_1 of 3D-GA shell ($n = 1$, $k = 8\,\mathrm{m}^{-1}$, $N_p = 0\,\mathrm{N}$, $k_w = 0\,\mathrm{N/m^3}$, $k_p = 0\,\mathrm{N/m}$): the first L-R-C mode (top left), the second L-R-C mode (top right), and the third L-R-C mode (bottom).

The influence of applied force N_p on the dispersion relations of the 3D-GA shell is plotted in Figure 9. For all the porosity distributions, the phase velocities initially increase slightly, then increase rapidly, and finally approach to constant. This interesting phenomenon indicates that the applied force has significant effect on the dispersion relation in certain range; beyond this range, however, it affects slightly the dispersion relation.

Figure 10 illustrates the effect of spring constant k_w on the dispersion relations of 3D-GA shells with different porosity distributions. It is interesting that a similar variation tendency of phase velocity can be observed with the comparison of Figure 9. In certain range, spring constant has significant influence on the phase velocity but it is insignificant for phase velocity beyond this range. For example, the phase velocity for the first L-R-C mode changes rapidly when $10^{11}\,\mathrm{N/m^3} \le k_w \le 10^{13}\,\mathrm{N/m^3}$, while it almost remains constant if $k_w < 10^{11}\,\mathrm{N/m^3}$ or $k_w > 10^{13}\,\mathrm{N/m^3}$.

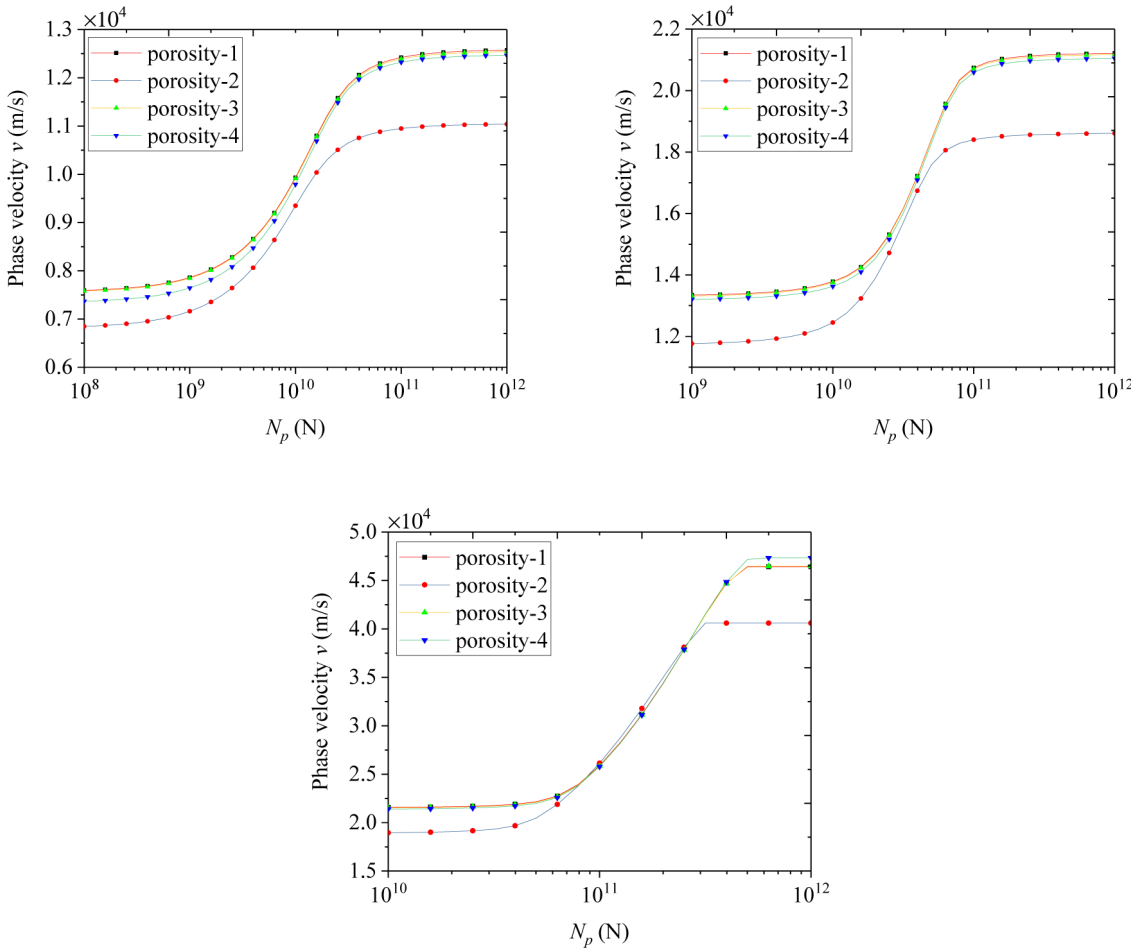

Figure 9. Phase velocity versus applied force N_p of 3D-GA shell ($e_1 = 0.5$, $n = 1$, $k = 8\,\mathrm{m}^{-1}$, $k_w = 0\,\mathrm{N/m}^3$, $k_p = 0\,\mathrm{N/m}$): the first L-R-C mode (top left), the second L-R-C mode (top right), and the third L-R-C mode (bottom).

Figure 11 examines the effect of shear constant k_p on the dispersion relations of the 3D-GA shell. When the shear constant is in the certain range, it has conspicuous effect on the phase velocity of the 3D-GA shell. From Figures 9–11, it is concluded that the applied force, spring constant and shear constant have similar influence on the phase velocity of 3D-GA shells. Such observations are significant for guiding the structural design of 3D-GA shells by adjusting the corresponding parameters.

In Figure 12, phase velocity versus radius-to-thickness ratio r/h of the 3D-GA shell is depicted. It is found that the phase velocities for the L-R-C modes initially decrease rapidly and then tend to be constant. In particular, the phase velocities for the second and third L-R-C modes decrease faster than that for the first L-R-C mode. Additionally, it is worth mentioning that when $r/h > 15$, the phase velocities are insensitive to the radius-to-thickness ratio.

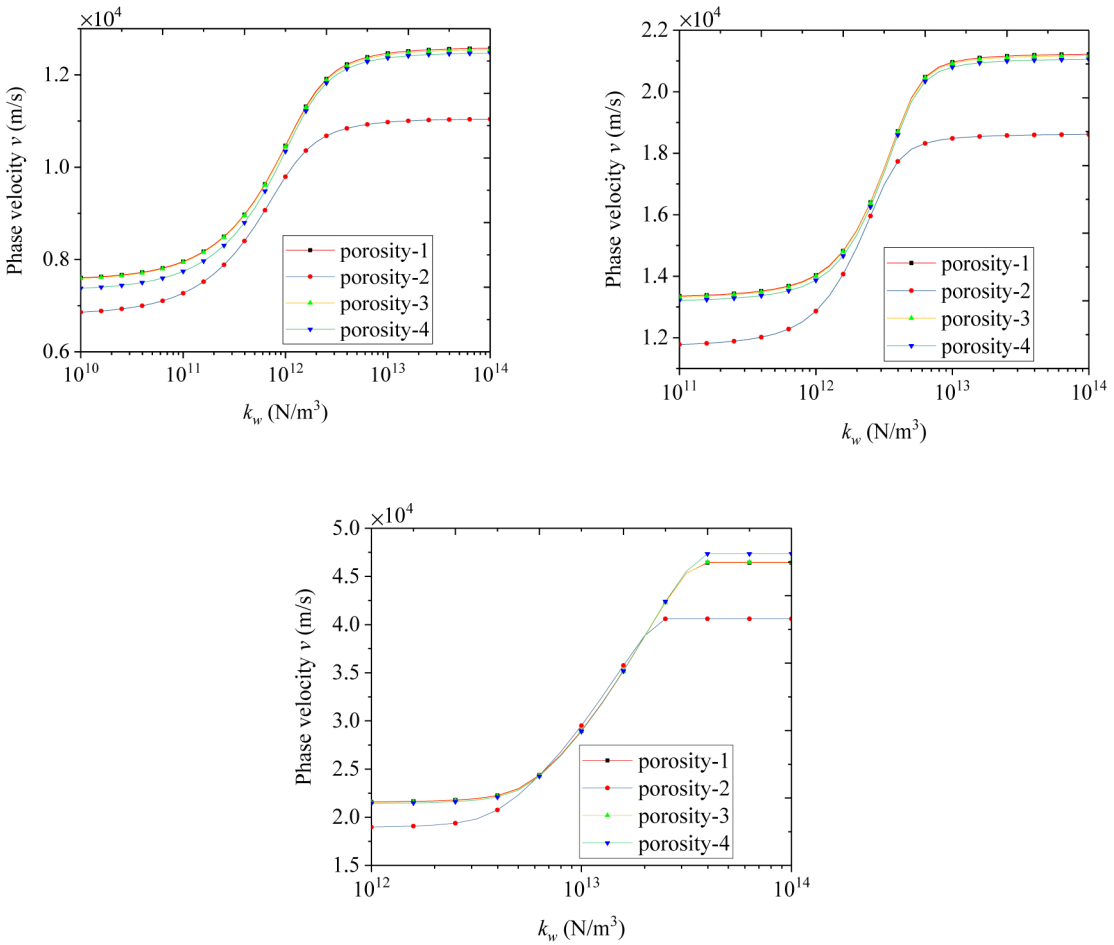

Figure 10. Phase velocity versus spring constant k_w of 3D-GA shell ($e_1 = 0.5$, $n = 1$, $k = 8\,\mathrm{m}^{-1}$, $N_p = 0\,\mathrm{N}$, $k_p = 0\,\mathrm{N/m}$): the first L-R-C mode (top left), the second L-R-C mode (top right), and the third L-R-C mode (bottom).

5. Concluding remarks

Wave propagation characteristics in 3D-GA cylindrical shells are studied in the framework of the FSD shell theory. Hamilton's principle is utilized to derive the governing equations. The effects of longitudinal and circumferential wave numbers, the porosity distribution, the porosity coefficient, the applied forces, the Winkler–Pasternak elastic foundation and the radius-to-thickness ratio on wave dispersion relations of 3D-GA shells are investigated. The main conclusions are summarized as follows:

(1) An increasing porosity coefficient leads to a decrease in the phase velocities of 3D-GA shells. Among different types of porosity distribution, the porosity-1 shell has the largest phase velocity whereas the porosity-2 shell has the smallest phase velocity.

(2) For the L-R-C modes of 3D-GA shells, the phase velocities show nonlinear variation with the change of longitudinal and circumferential wave numbers. It is found that phase velocities of the three L-R-C modes approach to constant and are close to each other when the longitudinal wave number is large.

(3) As the applied forces, the spring constant and the shear constant increase, the phase velocities of 3D-GA shells initially increase slightly, then increase rapidly, and finally approach to constant.

(4) With the increase in radius-to-thickness ratio, the phase velocities of 3D-GA shells initially decrease rapidly but finally are insensitive to the radius-to-thickness ratio.

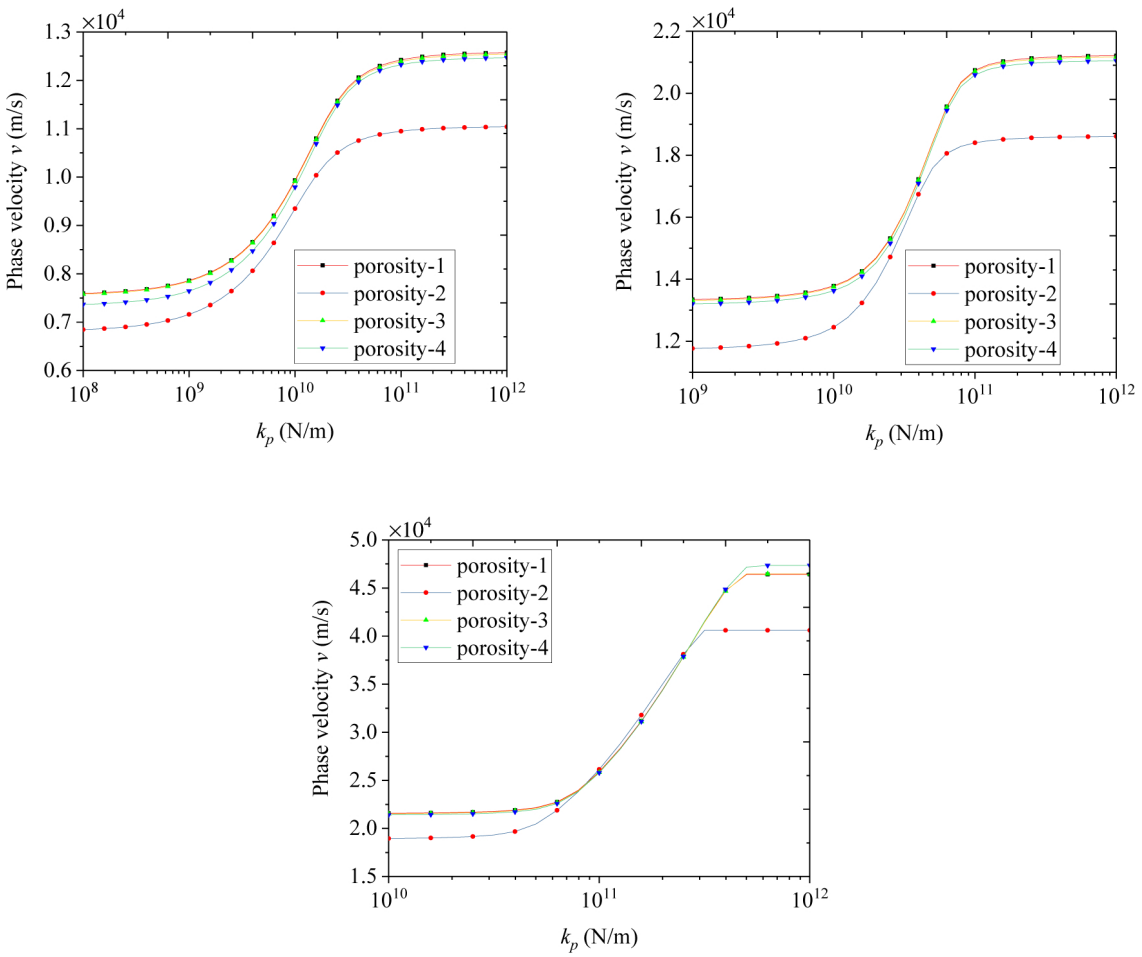

Figure 11. Phase velocity versus shear constant k_p of 3D-GA shell ($e_1 = 0.5$, $n = 1$, $k = 8\,\mathrm{m}^{-1}$, $N_p = 0\,\mathrm{N}$, $k_w = 0\,\mathrm{N/m}^3$): the first L-R-C mode (top left), the second L-R-C mode (top right), and the third L-R-C mode (bottom).

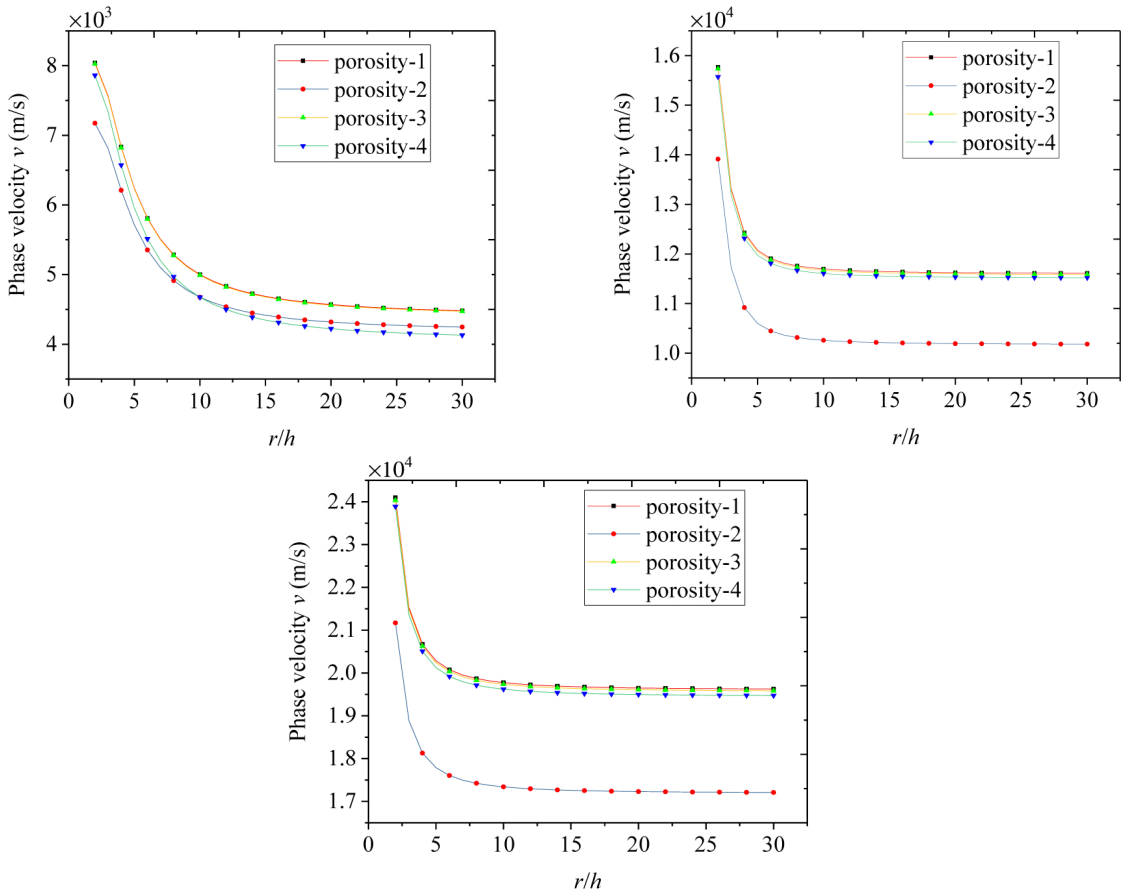

Figure 12. Phase velocity versus radius-to-thickness ratio r/h of 3D-GA shell ($e_1 = 0.5$, $n = 1$, $k = 8\,\mathrm{m}^{-1}$, $N_p = 0\,\mathrm{N}$, $k_w = 0\,\mathrm{N/m^3}$, $k_p = 0\,\mathrm{N/m}$): the first L-R-C mode (top left), the second L-R-C mode (top right), and the third L-R-C mode (bottom).

Appendix A

$$A_{11} = \int_{-h/2}^{h/2} \frac{E(z)}{1-\mu^2}\,\mathrm{d}z \qquad A_{12} = \int_{-h/2}^{h/2} \frac{E(z)}{1-\mu^2} z\,\mathrm{d}z \qquad A_{13} = \int_{-h/2}^{h/2} \frac{\mu E(z)}{1-\mu^2}\,\mathrm{d}z \qquad A_{14} = \int_{-h/2}^{h/2} \frac{\mu E(z)}{1-\mu^2} z\,\mathrm{d}z$$

$$B_{11} = \int_{-h/2}^{h/2} G(z)\,\mathrm{d}z \qquad B_{12} = \int_{-h/2}^{h/2} G(z) z\,\mathrm{d}z \qquad C_{11} = A_{12} \qquad C_{12} = \int_{-h/2}^{h/2} \frac{E(z)}{1-\mu^2} z^2\,\mathrm{d}z$$

$$C_{13} = A_{14} \qquad C_{14} = \int_{-h/2}^{h/2} \frac{\mu E(z)}{1-\mu^2} z^2\,\mathrm{d}z \qquad D_{11} = B_{12} \qquad D_{12} = \int_{-h/2}^{h/2} G(z) z^2\,\mathrm{d}z$$

Appendix B

$$L_{11} = A_{11}k^2r^2 + B_{11}n^2 \qquad L_{12} = (A_{13} + B_{11})\,knr \qquad L_{13} = -\mathrm{i}A_{13}kr$$

$$L_{14} = A_{12}k^2r^2 + B_{12}n^2 \qquad L_{15} = (A_{14} + B_{12})\,knr \qquad L_{21} = (A_{13} + B_{11})\,knr$$

$$L_{22} = A_{11}n^2 + B_{11}k^2r^2 + \kappa_s B_{11} \qquad L_{23} = -\mathrm{i}n(A_{11} + \kappa_s B_{11}) \qquad L_{24} = (A_{14} + B_{12})\,knr$$
$$L_{25} = A_{12}n^2 - \kappa_s B_{11}r + B_{12}k^2r^2 \qquad L_{31} = \mathrm{i}A_{13}\,kr \qquad L_{32} = \mathrm{i}n(A_{11} + \kappa_s B_{11})$$
$$L_{33} = A_{11} + \kappa_s B_{11}(n^2 + k^2r^2) + N_{px}k^2r^2 + N_{p\theta}n^2 + k_w r^2 + k_p(n^2 + k^2r^2)$$
$$L_{34} = \mathrm{i}(A_{14} - \kappa_s B_{11}r)\,kr \qquad L_{35} = \mathrm{i}n(A_{12} - \kappa_s B_{11}r) \qquad L_{41} = C_{11}k^2r^2 + D_{11}n^2$$
$$L_{42} = (C_{13} + D_{11})\,knr \qquad L_{43} = \mathrm{i}(\kappa_s B_{11}r - C_{13})\,kr \qquad L_{44} = \kappa_s B_{11}r^2 + C_{12}k^2r^2 + D_{12}n^2$$
$$L_{45} = (C_{14} + D_{12})\,knr \qquad L_{51} = (C_{13} + D_{11})\,knr \qquad L_{52} = -\kappa_s B_{11}r + C_{11}n^2 + D_{11}k^2r^2$$
$$L_{53} = \mathrm{i}n(\kappa_s B_{11}r - C_{11}) \qquad L_{54} = (C_{14} + D_{12})\,knr \qquad L_{55} = \kappa_s B_{11}r^2 + C_{12}n^2 + D_{12}k^2r^2$$

$$H_{11} = I_1r^2 \quad H_{14} = I_2r^2 \quad H_{12} = H_{13} = H_{15} = 0 \qquad H_{21} = H_{23} = H_{24} = 0$$
$$H_{22} = I_1r^2 \quad H_{25} = I_2r^2 \quad H_{31} = H_{32} = H_{34} = H_{35} = 0 \quad H_{33} = I_1r^2$$
$$H_{41} = I_2r^2 \quad H_{44} = I_3r^2 \quad H_{42} = H_{43} = H_{45} = 0 \qquad H_{51} = H_{53} = H_{54} = 0$$
$$H_{52} = I_2r^2 \quad H_{55} = I_3r^2$$

Acknowledgements

This research was supported by the National Natural Science Foundation of China (Grant nos. 11922205 and 11672071), LiaoNing Revitalization Talents Program (Grant no. XLYC1807026), and the Fundamental Research Funds for the Central Universities (Grant no. N2005019).

References

[Aifantis 2016] E. C. Aifantis, "Internal length gradient (ILG) material mechanics across scales and disciplines", pp. 1–110 in *Advances in applied mechanics*, 1st ed., vol. 49, Elsevier, 2016.

[Aminipour et al. 2018] H. Aminipour, M. Janghorban, and L. Li, "A new model for wave propagation in functionally graded anisotropic doubly-curved shells", *Compos. Struct.* **190** (2018), 91–111.

[Askes and Aifantis 2009] H. Askes and E. C. Aifantis, "Gradient elasticity and flexural wave dispersion in carbon nanotubes", *Phys. Rev. B* **80**:19 (2009), 195412.

[Bi et al. 2012] H. Bi et al., "Spongy graphene as a highly efficient and recyclable sorbent for oils and organic solvents", *Adv. Funct. Mater.* **22**:21 (2012), 4421–4425.

[Chatterjee et al. 2012] S. Chatterjee et al., "Mechanical reinforcement and thermal conductivity in expanded graphene nanoplatelets reinforced epoxy composites", *Chem. Phys. Lett.* **531** (2012), 6–10.

[Chen et al. 2011] Z. Chen et al., "Three-dimensional flexible and conductive interconnected graphene networks grown by chemical vapour deposition", *Nat. Mater.* **10**:6 (2011), 424–428.

[Chen et al. 2014] S. Chen et al., "Hierarchical 3D mesoporous silicon@graphene nanoarchitectures for lithium ion batteries with superior performance", *Nano Res.* **7**:1 (2014), 85–94.

[Chen et al. 2015] D. Chen, J. Yang, and S. Kitipornchai, "Elastic buckling and static bending of shear deformable functionally graded porous beam", *Compos. Struct.* **133** (2015), 54–61.

[Dai and Wang 2005] H. L. Dai and X. Wang, "Stress wave propagation in laminated piezoelectric spherical shells under thermal shock and electric excitation", *Struct. Eng. Mech.* **24**:2 (2005), 263–276.

[Geim 2009] A. K. Geim, "Graphene: status and prospects", *Science* **324**:5934 (2009), 1530–1534.

[Geim and Novoselov 2009] A. K. Geim and K. S. Novoselov, "The rise of graphene", pp. 11–19 in *Nanoscience and technology: a collection of reviews from Nature journals*, 2009.

[Hu et al. 2008] Y.-G. Hu et al., "Nonlocal shell model for elastic wave propagation in single- and double-walled carbon nanotubes", *J. Mech. Phys. Solids* **56**:12 (2008), 3475–3485.

[Huang et al. 2012] X. Huang et al., "Functional nanoporous graphene foams with controlled pore sizes", *Adv. Mater.* **24**:32 (2012), 4419–4423.

[Jabbari et al. 2014] M. Jabbari, A. Mojahedin, A. R. Khorshidvand, and M. R. Eslami, "Buckling analysis of a functionally graded thin circular plate made of saturated porous materials", *J. Eng. Mech.* (*ASCE*) **140**:2 (2014), 287–295.

[Jiang and Fan 2014] L. Jiang and Z. Fan, "Design of advanced porous graphene materials: from graphene nanomesh to 3D architectures", *Nanoscale* **6**:4 (2014), 1922–1945.

[Kuang et al. 2013] J. Kuang et al., "A hierarchically structured graphene foam and its potential as a large-scale strain-gauge sensor", *Nanoscale* **5**:24 (2013), 12171.

[Lee et al. 2008] C. Lee, X. Wei, J. W. Kysar, and J. Hone, "Measurement of the elastic properties and intrinsic strength of monolayer graphene", *Science* **321**:5887 (2008), 385–388.

[Li et al. 2013] N. Li et al., "Three-dimensional graphene foam as a biocompatible and conductive scaffold for neural stem cells", *Sci. Rep.* **3** (2013), 1604.

[Li et al. 2014] Y. Li et al., "Highly compressible macroporous graphene monoliths via an improved hydrothermal process", *Adv. Mater.* **26**:28 (2014), 4789–4793.

[Liew and Wang 2007] K. M. Liew and Q. Wang, "Analysis of wave propagation in carbon nanotubes via elastic shell theories", *Int. J. Eng. Sci.* **45**:2-8 (2007), 227–241.

[Liu et al. 2011] C.-C. Liu, F.-M. Li, and W.-H. Huang, "Transient wave propagation and early short time transient responses of laminated composite cylindrical shells", *Compos. Struct.* **93**:10 (2011), 2587–2597.

[Lurie et al. 2018] S. A. Lurie et al., "Modeling the effective mechanical properties of "fuzzy fiber" composites across scales length", *Compos. B Eng.* **142** (2018), 24–35.

[Ma et al. 2018] L. H. Ma et al., "Wave propagation characteristics in magneto-electro-elastic nanoshells using nonlocal strain gradient theory", *Compos. Struct.* **199** (2018), 10–23.

[Magnucki and Stasiewicz 2004] K. Magnucki and P. Stasiewicz, "Elastic buckling of a porous beam", *J. Theor. Appl. Mech.* (*Warsaw*) **42**:4 (2004), 859–868.

[Novoselov et al. 2004] K. S. Novoselov et al., "Electric field effect in atomically thin carbon films", *Science* **306**:5696 (2004), 666–669.

[Pasternak 1954] P. L. Pasternak, *On a new method of analysis of an elastic foundation by means of two foundation constants*, Gosudarstvennoe Izdatelstvo Literaturi po Stroitelstvu I Arkhitekture, Moscow, 1954. in Russian.

[Qin et al. 2017] Z. Qin, G. S. Jung, M. J. Kang, and M. J. Buehler, "The mechanics and design of a lightweight three-dimensional graphene assembly", *Sci. Adv.* **3**:1 (2017), e160153.

[Qiu et al. 2017] L. Qiu et al., "Extremely low density and super-compressible graphene cellular materials", *Adv. Mater.* **29**:36 (2017), 1701553.

[Reddy 2004] J. N. Reddy, *Mechanics of laminated composite plates and shells: theory and analysis*, CRC press, 2004.

[Sha et al. 2016] J. Sha et al., "Preparation of three-dimensional graphene foams using powder metallurgy templates", *ACS Nano* **10**:1 (2016), 1411–1416.

[Sha et al. 2017] J. Sha et al., "Three-dimensional printed graphene foams", *ACS Nano* **11**:7 (2017), 6860–6867.

[Shakeri et al. 2006] M. Shakeri, M. Akhlaghi, and S. M. Hoseini, "Vibration and radial wave propagation velocity in functionally graded thick hollow cylinder", *Compos. Struct.* **76**:1-2 (2006), 174–181.

[Sorokin and Ershova 2004] S. V. Sorokin and O. A. Ershova, "Plane wave propagation and frequency band gaps in periodic plates and cylindrical shells with and without heavy fluid loading", *J. Sound Vib.* **278**:3 (2004), 501–526.

[Strek et al. 2017] W. Strek et al., "Laser induced white lighting of graphene foam", *Sci. Rep.* **7**:1 (2017), 41281.

[Sun and Aifantis 2014] B. Sun and E. C. Aifantis, "Gradient elasticity formulations for micro/nanoshells", *J. Nanomater.* **2014** (2014), 846370.

[Talebitooti and Choudari Khameneh 2017] R. Talebitooti and A. M. Choudari Khameneh, "Wave propagation across double-walled laminated composite cylindrical shells along with air-gap using three-dimensional theory", *Compos. Struct.* **165** (2017), 44–64.

[Thorp et al. 2005] O. Thorp, M. Ruzzene, and A. Baz, "Attenuation of wave propagation in fluid-loaded shells with periodic shunted piezoelectric rings", *Smart Mater. Struct.* **14**:4 (2005), 594–604.

[Vickery et al. 2009] J. L. Vickery, A. J. Patil, and S. Mann, "Fabrication of graphene-polymer nanocomposites with higher-order three-dimensional architectures", *Adv. Mater.* **21**:21 (2009), 2180–2184.

[Wang 2010] L. Wang, "Wave propagation of fluid-conveying single-walled carbon nanotubes via gradient elasticity theory", *Comput. Mater. Sci.* **49**:4 (2010), 761–766.

[Wang and Varadan 2007] Q. Wang and V. K. Varadan, "Application of nonlocal elastic shell theory in wave propagation analysis of carbon nanotubes", *Smart Mater. Struct.* **16**:1 (2007), 178–190.

[Wang et al. 2012] J. Wang et al., "Reinforcement with graphene nanosheets in aluminum matrix composites", *Scr. Mater.* **66**:8 (2012), 594–597.

[Wang et al. 2019] Y. Q. Wang, C. Ye, and J. W. Zu, "Nonlinear vibration of metal foam cylindrical shells reinforced with graphene platelets", *Aerosp. Sci. Technol.* **85** (2019), 359–370.

[Winkler 1867] E. Winkler, *Die lehre von der elastizität und festigkeit (The theory of elasticity and stiffness)*, H. Dominius, Prague, 1867.

[Wu et al. 2015] Y. Wu et al., "Three-dimensionally bonded spongy graphene material with super compressive elasticity and near-zero Poisson's ratio", *Nat. Commun.* **6**:1 (2015), 6141.

[Xu et al. 2008] K. Y. Xu, E. C. Aifantis, and Y. H. Yan, "Vibrations of double-walled carbon nanotubes with different boundary conditions between inner and outer tubes", *J. Appl. Mech.* (*ASME*) **75**:2 (2008), 021013.

[Xu et al. 2010] Y. Xu, K. Sheng, C. Li, and G. Shi, "Self-assembled graphene hydrogel *via* a one-step hydrothermal process", *ACS Nano* **4**:7 (2010), 4324–4330.

[Xu et al. 2014] K. Y. Xu et al., "Free transverse vibrations of a double-walled carbon nanotube: gradient and internal inertia effects", *Acta Mech. Solida Sin.* **27**:4 (2014), 345–352.

[Xu et al. 2016] X. Xu et al., "Naturally dried graphene aerogels with superelasticity and tunable Poisson's ratio", *Adv. Mater.* **28**:41 (2016), 9223–9230.

[Yang et al. 2018] J. Yang, D. Chen, and S. Kitipornchai, "Buckling and free vibration analyses of functionally graded graphene reinforced porous nanocomposite plates based on Chebyshev–Ritz method", *Compos. Struct.* **193** (February 2018), 281–294.

[Zeighampour and Beni 2017] H. Zeighampour and Y. T. Beni, "Size dependent analysis of wave propagation in functionally graded composite cylindrical microshell reinforced by carbon nanotube", *Compos. Struct.* **179** (2017), 124–131.

[Zeighampour et al. 2017] H. Zeighampour, Y. T. Beni, and I. Karimipour, "Wave propagation in double-walled carbon nanotube conveying fluid considering slip boundary condition and shell model based on nonlocal strain gradient theory", *Microfluid. Nanofluid.* **21**:5 (2017), 85.

[Zeighampour et al. 2018] H. Zeighampour, Y. Tadi Beni, and M. Botshekanan Dehkordi, "Wave propagation in viscoelastic thin cylindrical nanoshell resting on a visco-Pasternak foundation based on nonlocal strain gradient theory", *Thin-Walled Struct.* **122** (2018), 378–386.

[Zhen 2017] Y. X. Zhen, "Wave propagation in fluid-conveying viscoelastic single-walled carbon nanotubes with surface and nonlocal effects", *Physica E* **86** (2017), 275–279.

Received 24 Jun 2019. Revised 14 May 2020. Accepted 30 May 2020.

CHEN LIANG: neuliangchen@gmail.com
Department of Mechanics, Northeastern University, Shenyang 110819, China

YAN QING WANG: wangyanqing@mail.neu.edu.cn
Department of Mechanics, Northeastern University, Shenyang 110819, China

and

Key Laboratory of Ministry of Education on Safe Mining of Deep Metal Mines, Northeastern University, Shenyang 110819, China

JOURNAL OF MECHANICS OF MATERIALS AND STRUCTURES

msp.org/jomms

Founded by Charles R. Steele and Marie-Louise Steele

Cover photo: Mando Gomez, www.mandolux.com

See msp.org/jomms for submission guidelines.

JoMMS (ISSN 1559-3959) at Mathematical Sciences Publishers, 798 Evans Hall #6840, c/o University of California, Berkeley, CA 94720-3840, is published in 10 issues a year. The subscription price for 2020 is US $660/year for the electronic version, and $830/year (+$60, if shipping outside the US) for print and electronic. Subscriptions, requests for back issues, and changes of address should be sent to MSP.

JoMMS peer-review and production is managed by EditFLOW® from Mathematical Sciences Publishers.

PUBLISHED BY

mathematical sciences publishers

nonprofit scientific publishing

http://msp.org/

Journal of Mechanics of Materials and Structures
Volume 15, No. 4 July 2020